Volume 1 | Number 1 | Jan 2013 | Pages 1–100

Nanoscale

www.rsc.org/nanoscale

ROYAL SOCIETY OF CHEMISTRY

ROYAL SOCIETY OF CHEMISTRY

www.rsc.org/nanoscale

Journal Name

Nanoscale

Dynamic Article Links▶

ARTICLE TYPE

Cobalt nanoparticles embedded in N-doped carbon as an efficient bifunctional electrocatalyst for oxygen reduction and evolution reactions

Yunhe Su, Yihua Zhu,* Hongliang Jiang, Jianhua Shen, Xiaoling Yang, Wenjian Zou, Jianding Chen,* and Chunzhong Li

Cobalt based catalysts are promising bifunctional electrocatalysts for both oxygen reduction and oxygen evolution reactions (ORR and OER) in unitized regenerative fuel cells (URFCs) operating with alkaline electrolytes. Here we report a hybrid composite of cobalt nanoparticles embedded in nitrogen-doped
10 carbon (Co/N-C) via a solvothermal carbonization strategy. With the synergistic effect arised from the N-doped carbon and cobalt nanoparticles in the composite, the Co/N-C hybrid catalyst exhibits highly efficient bifunctional catalytic activity and excellent stability toward both ORR and OER. The ΔE (Oxygen electrode activity parameter for judging the overall electrocatalytic activity of a bifunctional electrocatalyst) value for Co/N-C is 0.859 V, which is smaller than Pt/C and most of the non-precious
15 metal catalysts in previous literatures. Furthermore, the Co/N-C composite also shows better bifunctional catalytic activity than its oxidative counterparts, which could be attributed to the high specific surface area and efficient charge transfer ability of the composite, as well as the good synergistic effect between N-doped carbon and the Co nanoparticles in the Co/N-C composite.

Introduction

20 With the increasing demand for clean and sustainable energy, great efforts have been devoted to alternative energy conversion and storage systems with high efficiency, low cost, and environmental benignity.[1,2] Electrocatalysts for oxygen reduction and oxygen evolution reactions (ORR and OER) are undoubtedly
25 the key point for various renewable energy technologies, including fuel cells, metal-air batteries, and water splitting.[3-5] The ORR is the ubiquitous cathode reaction in fuel cells and metal-air batteries, while the OER is the anode reaction employed in electrolysis cells and plays an important role in energy storage
30 such as solar fuel synthesis and water splitting.[6-8]

A unitized regenerative fuel cell (URFC) is a promising energy storage system that works as a fuel cell consuming H_2 and in reverse as a water electrolyzer producing H_2 and O_2.[6,9] Bifunctional catalysts with high activities for both ORR and OER
35 are needed in this system to catalyze the process. Up to now, Pt and its alloys have long been regarded as the most efficient catalysts for ORR. However, their high cost and poor durability severely hinder their applicability to broad commercialization. In addition, Pt has only moderate activity for the OER, which is not
40 satisfactory when used as a bifunctional electrocatalyst in URFC. Ruthenium (Ru) and iridium (Ir) oxides are considered as the best known OER catalysts, nevertheless, these metals suffer from the scarcity and high cost of the precious metals and are not as active for the ORR as Pt.[10-12] Therefore, it is highly challenging but
45 desirable to develop efficient bifunctional electrocatalysts with low cost and superior durability for both ORR and OER to replace conventional precious metals utilized in URFC.

In the past decades, although various non-precious materials exhibit excellent catalytic activity for ORR[13] or OER,[14] the
50 bifunctional electrocatalysts for both ORR and OER are still rarely reported. First row transition metal chalcogenides, such as oxides,[15] sulfides,[16] and selenides,[17] have been extensively studied as ORR catalysts, but only transition metal oxides, especially single or complex oxides of Mn, Co and Ni were
55 studied as bifunctional electrocatalysts in alkaline solution. For instance, nanostructured MnO_2 and various nanostructured $NiCo_2O_4$ demonstrated effective bifunctional catalytic activities in alkaline media.[6,11,18,19] However, most of these reported bifunctional electrocatalysts suffer from limited catalytic
60 activities due to their small specific surface area and low conductivities. Loading of transition metal oxides on conducting carbon supports can overcome the limitations and improve the bifunctional catalytic activity. In this way, it is encouraging and significant to study the bifunctional catalytic activities of hybrid
65 composites composed of carbon materials and transition metal oxides. And some hybrid composites consisting of carbon materials (or N-doped carbon materials) and cobalt oxides have been developed to serve as efficient bifunctional electrocatalysts in alkaline solution.[2,5,20-23] In these studies, the carbon materials
70 play key roles in enhancing the catalytic activities of these hybrid composites. However, despite abundant research on cobalt oxides or sulfides,[24-32] there were few reports on cobalt nanoparticles (Co NPs) based bifunctional electrocatalyst for both ORR and OER. And as far as we know, a hybrid material composed of Co
75 NPs and nitrogen-doped carbon has not yet been investigated as a

bifunctional electrocatalyst, presumably due to the easily agglomerating of Co NPs and their poor chemical and thermal stabilities.[33, 34]

In this study, we prepared a hybrid composite of Co NPs embedded in N-doped carbon (Co/N-C-800) via a solvothermal carbonization strategy. With the synergistic effect arised from the N-doped carbon and Co NPs in Co/N-C-800 composite, the hybrid composite shows highly efficient bifunctional catalytic activity and excellent stability for both ORR and OER in alkaline solution. Furthermore, the Co/N-C-800 composite also shows better bifunctional catalytic activity than its oxidative counterparts, which could be attributed to the high specific surface area and efficient charge transfer ability of the composite, as well as the good synergistic effect between N-doped carbon and Co NPs in Co/N-C-800 composite.

Experimental

Instrumentation and Chemicals.

X-ray diffraction (XRD) patterns were carried out on a powder X-ray diffractometer (RIGAK, D/MAX 2550 VB/PC, Japan). Scanning electron microscopy (SEM) images were recorded on the S-4800 field emission scanning electron microscope equipped with an energy dispersive X-ray analyzer (EDX). Transmission electron microscopy (TEM) studies were performed on a JEM-2100 high-resolution transmission electron microscope. X-ray photoelectron spectroscopy (XPS) was conducted using a VG ESCA 2000 with an Mg Kα as the source and using the C 1s peak at 284.6 eV as an internal standard. Thermogravimetric analysis (TGA) of sample was performed on a SDT-Q600 simultaneous TGA/DSC thermogravimetric analyzer (TA Instruments), and the sample was heated under air atmosphere from room temperature to 900 ^{o}C at 10 ^{o}C min^{-1}. Brunauer–Emmett–Teller (BET) and Barrett–Joyner–Halenda (BJH) models were used to determine the specic surface areas, pore volume, and pore sizes of the samples, respectively. Raman spectra were collected on a Bruker RFS 100/S spectrometer with 514 nm laser excitation. Electrochemical experiments were carried out with the CHI660C electrochemical workstation (CH Instrument Co., China). All chemicals were of analytical grade and used without further purification. Ultrapure water ($\geq$ 18MΩ cm^{-1}) was used throughout.

Materials Synthesis.

Synthesis of Co/N-C composites: Cobalt acetate tetrahydrate (Co(Ac)$_2$·4H$_2$O) (0.498 g, 2.0 mmol) was first dissolved in anhydrous ethanol (65 mL), dopamine hydrochloride (0.379 g, 2.0 mmol) was dispersed in ultrapure water (5 mL) and then injected into the above solution, followed by the addition of 2.0 mL NH$_4$OH (30% solution). The reaction was kept at room temperature with stirring for 45 min. After that, the reaction mixture was transferred to a 100 mL autoclave for hydrothermal reaction at 150 ^{o}C for 4 h. The precipitates were collected by centrifugation and washed with ultrapure water and anhydrous ethanol for several times. After drying, the resulting powder was heated to the targeted carbonization temperature (700, 800 and 900 ^{o}C) at a rate of 5 ^{o}C min^{-1} under flowing argon gas and maintained at this temperature for 2 h. After cooling down to room temperature, the resultant Co/N-C samples were collected for further uses.

Synthesis of N-doped carbon: The N-doped carbon was prepared following a reported method.[35] Typically, ammonia aqueous solution (NH$_4$OH, 1 mL, 28-30%) was mixed with ethanol (40 mL) and deionized water (90 mL) under mild stirring at room temperature for 30 min. Dopamine hydrochloride (0.5 g) was dissolved in deionized water (10 mL) and then injected into the above mixture solution. The reaction was allowed to proceed for 30 h. Then the precipitates were collected by centrifugation and washed with ultrapure water for three times, and finally dried at 60 ^{o}C overnight. After that, the N-doped carbon was obtained by carbonizing the dried powder at 800 ^{o}C for 2 h in Ar at a rate of 5 ^{o}C min^{-1}.

Synthesis of pristine Co NPs: Here the pristine Co NPs were synthesized as reported.[34] First, a mixture containing oleic acid (0.35 mL), dioctylamine (0.5 mL) and 1,2,3,4-tetrahydrophthalene (18 mL) was heated at 110 ^{o}C for 0.5 h under Ar protection and then cooled down to room temperature. Co$_2$(CO)$_8$ (0.54 g) was quickly added into the above solution and the mixture was reheated to 100 ^{o}C for 30 min, followed by rapidly heating to 208 ^{o}C for 30 min at the heating rate of 15 ^{o}C/min under Ar protection. After cooled to room temperature, the obtained Co NPs were precipitated by adding 60 mL of ethanol. The product was separated by centrifugation at 9000 rpm for 10 min. The Co NPs were dispersed in hexane before use.

Thermal conversion of Co/N-C: Typically, the obtained Co/N-C-800 composite was thermally treated under ambient air in a muffle oven. The black powder was homogeneously dispersed in a ceramic disk. The ceramic disk was heated at the desired temperatures (250 or 450 ^{o}C) for 90 min with a heating rate of 1 ^{o}C min^{-1}. The obtained samples (Co/N-C-800-250 or Co/N-C-800-450) were collected for further characterizations.

Electrode Preparation and Electrochemical Tests.

The preparation method of the working electrodes containing investigated catalysts can be found as follow.[36] In short, 5 mg of catalyst powder was dispersed in 1 mL of 3:1 (v/v) water/2-propanol mixed solvent with 40 μL of Nafion solution (5 wt%, Sigma-Aldrich), and then the mixture was ultrasonicated for about 1 h to generate a homogeneous ink. Next, 10 μL of the dispersion was transferred onto the glassy carbon rotating disk electrode (RDE) (5 mm in diameter, Pine Research Instrumentation), leading to the catalyst loading ~0.25 mg cm^{-2}. Finally, the as-prepared catalyst film was dried at room temperature for electrochemical measurement.

All electrochemical tests, including cyclic voltammograms (CVs), linear sweep voltammetrys (LSVs), chronoamperometry and electrochemical impedance spectroscopy (EIS), were performed at room temperature in 0.1 M KOH aqueous solution (pH = 13), which were purged with N$_2$ or O$_2$ for at least 30 min prior to each measurement. The glassy carbon rotating disk electrode coated with catalyst was used as working electrode, a platinum wire and Ag/AgCl (3.5 M KCl) electrode served as counter and reference electrodes, respectively. All the potentials versus the Ag/AgCl (3.5 M KCl) reference electrode were converted to the reversible hydrogen electrode (RHE) scale via the Nernst equation:

$$E_{RHE} = E_{Ag/AgCl} + 0.0591pH + E^{\theta}_{Ag/AgCl} \qquad (1)$$

where E_{RHE} is the converted potential versus RHE, $E_{Ag/AgCl}$ is the experimental potential measured against the Ag/AgCl reference electrode, and $E^{\theta}_{Ag/AgCl}$ is the standard potential of Ag/AgCl (3.5 M KCl) at 25 °C (0.205 V). The electrochemical measurements were carried out in 0.1 M KOH (pH = 13) at room temperature: therefore, $E_{RHE} = E_{Ag/AgCl} + 0.973$ V.

ORR measurement: CVs were scanned at a scan rate of 50 mV s⁻¹, and LSVs were recorded at various rotating speeds from 400 to 1600 rpm at a scan rate of 10 mV s⁻¹. Chronoamperometry tests were conducted in O_2-saturated 0.1 M KOH at 0.55 V (vs. RHE) with a rotation rate of 900 rpm. The exact kinetic parameters for the ORR activities, including electron transfer number (n) and kinetic current density (J_k) were investigated based on the Koutecky-Levich (K-L) equation:[2, 37]

$$\frac{1}{J} = \frac{1}{J_L} + \frac{1}{J_K} = \frac{1}{B\omega^{1/2}} + \frac{1}{J_K} \tag{2}$$

$$B = 0.2nFC_0(D_0)^{2/3}\nu^{-1/6} \tag{3}$$

where J is the measured current density, J_k is the kinetic current density, and J_L is the diffusion current density; ω is the electrode rotation rate, F is the Faraday constant (96485 C mol⁻¹), C_0 is the bulk concentration of O_2 (1.2×10^{-6} mol cm⁻³), D_0 is the diffusion coefficient of O_2 (1.9×10^{-5} cm² s⁻¹), and ν is the kinetic viscosity of the electrolyte (0.01 cm² s⁻¹). Here the constant 0.2 is adopted when the rotating rate is expressed in rpm.

OER measurement: The polarization curves were obtained by sweeping the potential from 1.0 to 1.9 V (vs. RHE) with a sweep rate of 10 mV s⁻¹ at 1600 rpm. The OER potential was IR corrected using E - iR relation, where i is the current and R is the uncompensated electrolyte ohmic resistance, which was measured via high-frequency AC impedance. The accelerated stability tests for OER were performed in O_2-saturated 0.1 M KOH at room temperature by potential cycling between 1.25 V and 1.85 V (vs. RHE) at a sweep rate of 100 mV s⁻¹ for 500 cycles. At the end of the cycles, the resulting electrodes were used for polarization curves at a sweep rate of 10 mV s⁻¹.

Electrochemical impedance spectroscopy (EIS) was carried out in the frequency range of 1 MHz to 0.1 Hz with an excitation amplitude of 10 mV.

Results and discussion

In this work, similar to our previously reported method,[38] we develop a solvothermal carbonization strategy to in situ prepare hybrid composite of Co/N-C. The fabrication process of Co/N-C using dopamine and Co(Ac)₂ as precursors is illustrated in Scheme 1 together with the predicted microstructure of the N-doped carbon in Co/N-C. Herein, dopamine is self-polymerized in a mixture containing water, ethanol, and ammonia during the solvothermal treatment. Meanwhile, the resulting polydopamine that inherits functional groups such as catechol and N-H groups could effectively absorb Co^{2+} ions. Owing to the good solubility of dopamine and Co^{2+} ions in the mixed solvent of water and ethanol, the Co species could be uniformly formed and well embedded into polydopamine during the solvothermal process. Therefore, in the pyrolysis step, the in situ introduction of Co NPs into the N-doped carbon matrix could be successfully achieved.
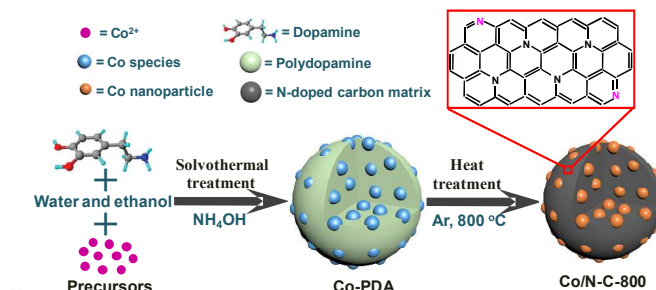
Scheme 1. Illustration of the fabrication process for Co/N-C-800, and the possible microstructures of the N-doped carbon in Co/N-C-800.

For the Co/N-C composites pyrolyzed under different temperatures (700, 800 and 900 °C), TEM images show that the Co NPs are uniformly distributed in the carbon matrix and that the sized gradually increase with increasing treatment temperatures (Supporting Information, Figure S1). As assessed by nitrogen adsorption-desorption measurements (Supporting Information, Figure S2), the composites are mesoporous with apparent specific BET surface areas of 246, 220 and 199 m² g⁻¹ for Co/N-C-700, Co/N-C-800 and Co/N-C-900 samples, respectively. Obviously, the small sized Co NPs and high specific surface area would be conducive to improving the catalytic activity of Co/N-C samples. However, the graphitization degree of carbon in the Co/N-C samples increases with the elevated pyrolysis temperatures, as indicated by the increased I_G/I_D ratios in the Raman spectra (Supporting Information, Figure S3). For N-doped carbon, it has been demonstrated that graphitic N can contribute to enhancing the ORR catalytic activity, especially in increasing the limiting current density.[39-41] Therefore, in this study, the pyrolysis temperature could play an active role in the catalytic activities of the Co/N-C samples. To select the optimal pyrolysis temperature, we carried out RDE measurements at 1600 rpm in O_2-saturated 0.1 M KOH solution for the Co/N-C samples carbonized under different temperatures to evaluate their ORR and OER activities (Supporting Information, Figure S4). As depicted in Figure S4, both the ORR and OER activities for the Co/N-C samples increased with increasing the treatment temperature from 700 °C to 800 °C, but decreased when the temperature further increased to 900 °C. Therefore we choose 800 °C as the optimal pyrolysis temperature, and select the Co/N-C-800 catalyst for more detailed studies.
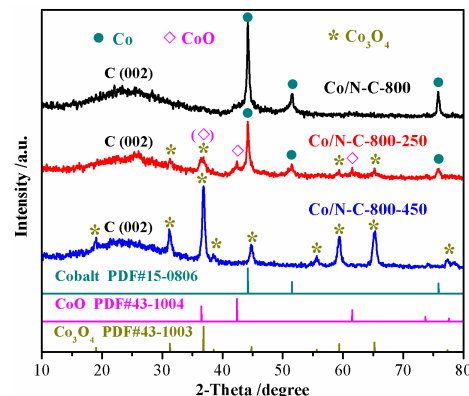

Fig. 1 XRD patterns of Co/N-C samples and the JCPDS cards #15-0806, #43-1004, #43-1003 for the corresponding metallic cobalt, CoO, Co₃O₄, respectively.

The X-ray diffraction (XRD) pattern of Co/N-C-800 composite in Fig. 1 shows a broad C (002) diffraction peak and the well-defined peaks at around 44.3°, 51.6°, 75.8°, which are in good agreement with JCPDS card 15-0806, implying the presence of metallic cobalt in the Co/N-C-800 hybrid composite. It has been reported previously that a mild oxidation of the metallic cobalt nanoparticles in the carbon-cobalt hybrid composite can lead to a good bifunctional catalytic activity.[20] Then here the Co/N-C-800 composites were subjected to annealing treatment at 250 °C and 450 °C (denoted as Co/N-C-800-250 and Co/N-C-800-450) in air for 90 min as the control samples (Supporting Information, Figure S5). The XRD pattern of Co/N-C-800-250 exhibits XRD peaks that arise from Co_3O_4, CoO and some remaining cobalt metals, indicating partially oxidization of the metallic cobalt in Co/N-C-800 hybrid composite after the second thermal treatment at 250 °C in air. While the Co/N-C-800-450 displayed well defined peaks corresponding to the JCPDS card 43-1003, which suggests the complete conversion of metallic cobalt to Co_3O_4 after the second thermal treatment at 450 °C in air.
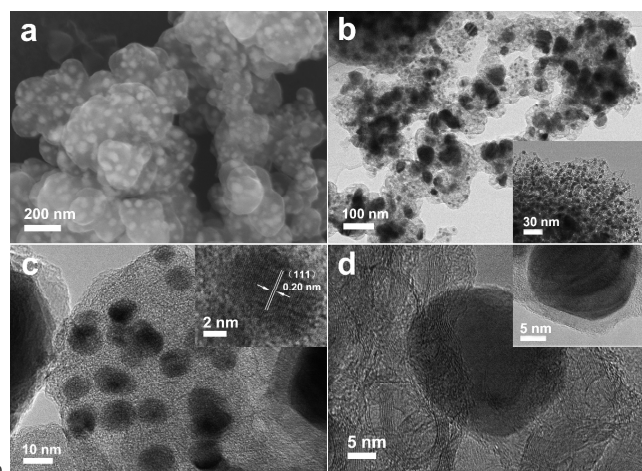

Fig. 2 (a) SEM and (b) TEM images of Co/N-C-800, inset of (b) shows the smaller sized Co nanoparticles incorporated in carbon layers; HRTEM images of (c) the smaller sized Co nanoparticles and (d) the graphitized carbon in Co/N-C-800, inset of (c) shows the crystal fringes of a single Co nanoparticle, inset of (d) shows a single Co nanoparticle surrounded by graphitized carbon.

The morphology and structure of Co/N-C-800 composite were examined by SEM and TEM studies. As shown in Fig. 2a, the SEM image of Co/N-C-800 reveals that the Co NPs are uniformly embedded in the granular-like carbon matrix, mainly with a size range of 20-50 nm. And the Co NPs are rarely aggregated, indicating a good dispersion in the carbon structure. The TEM image displays a similar result with the SEM image, except that many of smaller sized Co NPs (5-20 nm) incorporated in the carbon layers were also identified and observed (Fig. 2b, 2c and the inset from Fig. 2b). Such a structure of small sized Co NPs uniformly embedded in N-doped carbon matrix could effectively prevent the Co NPs from agglomerating and being excessively oxidized, and it might produce fast electron transport between the carbon matrix and the Co NPs, leading to efficient chemical performance.[42] The inset in Fig. 2c shows the high-resolution TEM (HRTEM) image focusing on a single Co nanoparticle, the crystal fringes were clearly displayed and the d-spacing of this Co nanoparticle was determined to be 0.20 nm, corresponding to the

spacing between (111) planes of nanocrystalline cobalt. Meanwhile, short-range ordered, graphitized carbon was also observed from the HRTEM image (Fig. 2d), the inset of Fig. 2d shows a Co nanoparticle surrounded by the graphitized carbon. It should be noted that the metallic transition metal or oxide phases within graphitized carbon shells are supposed to be conducive to greatly enhancing the catalytic activity of the catalysts, which has been reported in many previous researches.[10, 38, 43, 44] Then here it is also predictable that a similar mechanism may also work in our Co/N-C hybrid system due to the interaction between the small sized Co NPs and the N-doped graphitized carbon.
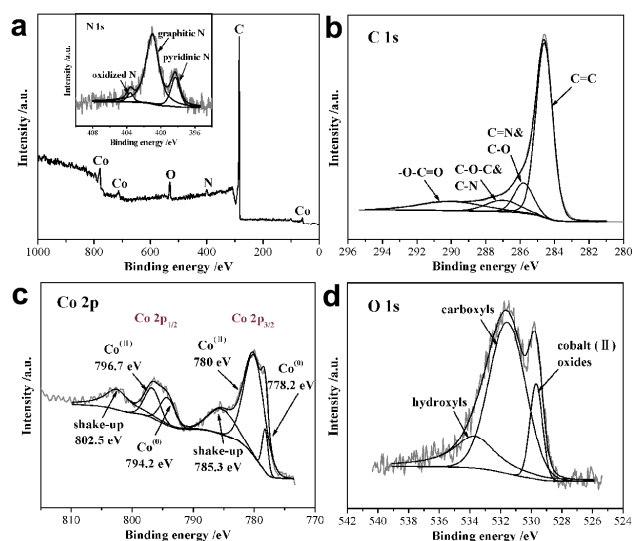

Fig. 3 (a) XPS spectrum of Co/N-C-800, inset shows the high-resolution spectrum of N 1s; high-resolution spectra of (b) C 1s, (c) Co 2p and (d) O 1s.

X-ray photoelectron spectroscopy (XPS) was used to investigate the elemental composition of Co/N-C-800. As shown in Fig. 3a, a set of peaks corresponding to C 1s (284.6 eV), N 1s (401.0 eV), O 1s (531.6 eV) and Co 2p (780.0 eV) are observed. The high-resolution XPS spectrum of the N 1s peak (inset of Fig. 3a) reveals pyridinic, graphitic and oxidized N species in Co/N-C-800, and the graphitic N dominates the majority. It has been reported that graphitic N could greatly increase the limiting current density, and pyridinic N could improve the onset potential, while other N species such as pyrrolic N or oxidized N had little effect on the electrochemical performance of N-doped carbon materials.[39] Moreover, some previous literatures have reported that a larger amount of graphitic N than pyridinic N is considered to be favourable for ORR.[40, 41] Thus, the enriched graphitic N-doped carbon in this work might have a positive effect on the ORR activity of Co/N-C-800. The deconvolution of C1s spectrum displays three types of C species: 66.5% C=C, 12.6% C=N & C-O, 8.3% C-O-C & C-N, and 12.6% -O-C=O, indicating the existence of carbon atoms connected to N and O heteroatoms (Fig. 3b). The Co $2p_{3/2}$ and $2p_{1/2}$ high-resolution spectra are fitted with three components corresponding to Co(0), Co(II), and the shake-up (satellites) peaks (Fig. 3c). The first peak maximum is found at 778.2 eV, which is consistent with the Co $2p_{3/2}$ binding energy of Co in a zerovalent state. The second peak exhibits a maximum at 780.0 eV. This peak is attributed to Co in a 2+ valence state, in agreement with the Co $2p_{3/2}$ binding

energy of CoO that is generally given in the range of 780-780.9 eV.[45] The dominant existence of Co^{2+} oxides in the XPS analysis indicates that the Co NPs on the surface of Co/N-C-800 composite are severely oxidized. This is well-explained by the fact that the exposure of Co NPs to ambient air could cause the formation of thin CoO shell since the cobalt(0) nanoclusters are sensitive to aerobic atmosphere.[34, 46, 47] The peaks at around 795 eV in this spectrum corresponds to the Co $2p_{1/2}$ states. Moreover, the high-resolution O1s spectrum could be fitted into three peaks at 533.7, 531.6 and 529.7 eV, which corresponds to hydroxyls, carboxyls and the oxygen related to the cobalt (II) oxides, respectively (Fig. 3d).[48] Notably, on the basis of the assumption that all Co has transferred to Co_3O_4 and all C has been burnt out, thermogravimetric (TG) analysis reveals that the mass fraction of cobalt in Co/N-C-800 is about 60.8 wt% (Supporting Information, Figure S6), which is much higher than that calculated from XPS (ca. 10.9 wt% converted from the 2.5 at% of Co (Supporting Information, Table S1)). This is because XPS analysis is more sensitive to the surface chemical composition (ca. 5 nm), which could hardly detect the Co NPs deeply embedded in the N-doped carbon matrix (Fig. 2).[38, 49]
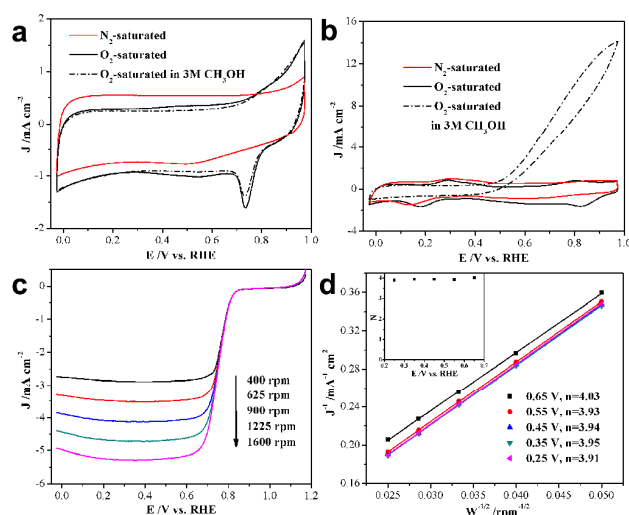

Fig. 4 CVs in N_2- and O_2-saturated 0.1 M KOH, in an O_2-saturated 0.1 M KOH upon the addition of CH_3OH (3 M) for (a) Co/N-C-800 and (b) Pt/C; (c) LSVs at different rotating speeds and (d) K-L plots for Co/N-C-800, inset of (d) shows the electron transfer number at different potentials.

To assess the ORR catalytic activity for Co/N-C-800 hybrid composite, cyclic voltammetry (CV) measurements were first carried out in O_2 versus N_2-saturated 0.1 M KOH aqueous solution at a scan rate of 50 mV s^{-1}. As shown in Fig. 4a, the Co/N-C-800 composite shows a distinct cathodic reduction peak at 0.733 V in O_2-saturated 0.1 M KOH solution, implying pronounced electrocatalytic activity of Co/N-C-800 for ORR. Furthermore, we also measured the catalytic selectivity of Co/N-C-800 and Pt/C against the electrooxidation of methanol in O_2-saturated 0.1 M KOH in the presence of methanol (3.0 M). The Pt/C shows a distinct response corresponding to methanol oxidation, with the disappearance of the cathodic reduction peak for ORR (Fig. 4b). In contrast, no noticeable change was observed for Co/N-C-800 under the same condition, indicating excellent selectivity of Co/N-C-800 than Pt/C (Fig. 4a). The good ORR selectivity and better tolerance to methanol crossover of

Co/N-C-800 than Pt/C could also be confirmed from the chronoamperometric measurements with the addition of 1.0 M methanol (Supporting Information, Fig. S7), which agrees well with the CV results in Fig. 4. To further investigate the ORR catalytic activity of Co/N-C-800, typical LSVs using a rotating disk electrode (RDE) in O_2-saturated 0.1 M KOH at various rotating speeds were recorded. As shown in Fig. 4c, the voltammetric profiles for Co/N-C-800 manifest typical increasing current density with higher rotation rates (from 400 to 1600 rpm). This result can be explained by shortened diffusion distance at high speeds, which is in accordance with other studies.[50-52] The corresponding Koutecky-Levich (K-L) plots (J^{-1} vs $W^{-1/2}$) under different electrode potentials shown in Fig. 4d are used to evaluate the transferred electron number per oxygen molecule in ORR. The K-L plots for Co/N-C-800 displays good linearity and their slopes remained almost constant over the potential range varying from 0.25 to 0.65 V, implying the transferred electron number per oxygen molecule in ORR at different electrode potentials were almost the same. Calculated from K-L equations, the transferred electron number per oxygen molecule in ORR on Co/N-C-800 electrode is 3.91, 3.95, 3.94, 3.93 and 4.03 at the potential of 0.25 V, 0.35 V, 0.45 V, 0.55 V and 0.65 V respectively, as depicted in the inset of Fig. 4d. These results suggest that the ORR for Co/N-C-800 electrode is a four-electron transfer process.
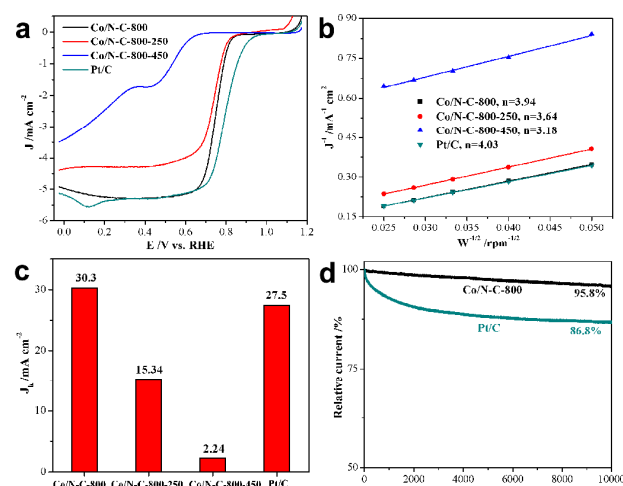

Fig. 5 (a) LSVs for Co/N-C samples and Pt/C; (b) K-L plots and (c) the corresponding J_k values at 0.45 V for Co/N-C samples and Pt/C; (d) I-t plots of Co/N-C-800 and Pt/C at 0.55 V.

To better compare and understand the ORR performance of Co/N-C samples, linear sweep voltammetry (LSV) measurements for Co/N-C-800, Co/N-C-800-250, Co/N-C-800-450, and the commercial Pt/C (20 wt% Pt) were performed on a rotating-disk electrode (RDE) in O_2-saturated 0.1 M KOH at a rotation rate of 1600 rpm. As shown in Fig. 5a, the Co/N-C-800 displays an onset potential of 0.834 V and current density of 5.26 mA cm^{-2} at 0.45 V, which is better than those of Co/N-C-800-250 (0.828 V and 4.26 mA cm^{-2}) and Co/N-C-800-450 samples (0.652 V and 1.66 mA cm^{-2}). Although the Co/N-C-800 composite shows a more negative onset potential, the current density at 0.45 V is comparable to Pt/C (0.936 V, 5.29 mA cm^{-2}), indicating an ORR activity close to the commercial Pt/C. To investigate the kinetic

differences in ORR catalysis on Co/N-C samples and Pt/C, the Tafel slopes, representing the overall resistance in the ORR process, were obtained according to linear plots of the LSVs at 1600 rpm for Co/N-C-800, Co/N-C-800-250, Co/N-C-800-450
5 and Pt/C (Supporting Information, Figure S8). The Co/N-C-800 shows a smaller Tafel slope of 61 mV/dec at low-overpotentials than those measured with Co/N-C-800-250 (68 mV/dec), Co/N-C-800-450 (80 mV/dec) and Pt/C (68 mV/dec) in 0.1 M KOH, indicating the more excellent ORR activity of Co/N-C-800.
10 Furthermore, such a slope close to the Nernstian Tafel slope (59 mV/dec) suggests that the rate-determining step of ORR might be the splitting of O-O bonds when two electrons transferred from active sites to adsorbed O_2 molecules.[53] Fig. 5b showed the Koutecky-Levich plots for Co/N-C-800, Co/N-C-800-250, Co/N-
15 C-800-450 and Pt/C at 0.45 V, the corresponding kinetic current density (J_k) calculated based on the K-L equation were also depicted in Fig. 5c. Significantly, the higher electron transfer number and the highest J_k value for Co/N-C-800 than those of other Co/N-C samples further manifest that a more efficient ORR
20 performance arises from the N-doped carbon supported Co nanoparticles composite.

Other than high activity, the long-term stability is another critical parameter that determines the practicability of catalyst. The durability tests for Co/N-C-800 and Pt/C were evaluated
25 using chronoamperometric measurements at 0.55 V (vs. RHE) in O_2-saturated 0.1 M KOH with a rotation rate of 900 rpm for 10000 s (Fig. 5d).[10, 38, 49] The Pt/C catalyst shows a 13.2% decrease in activity after 10000 s. As a comparison, Co/N-C-800 retains a high relative current of 95.8% after 10000 s, indicating
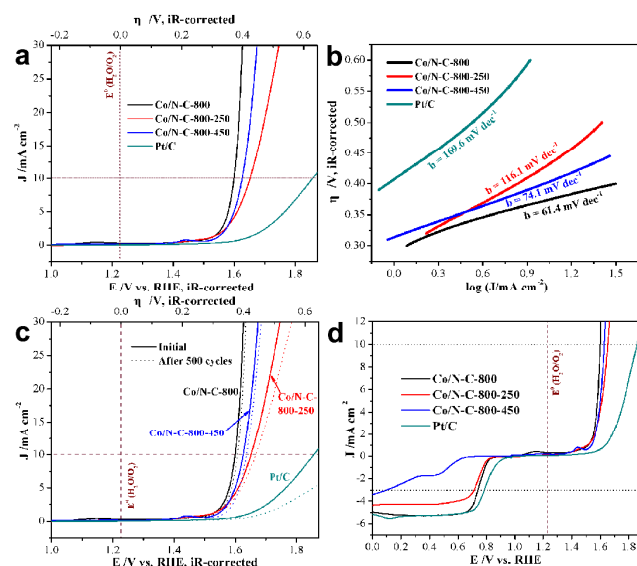30 the superior stability of Co/N-C-800 than the commercial Pt/C catalyst in alkaline environment.

Fig. 6 (a) Oxygen evolution currents for Co/N-C samples and Pt/C; (b) Tafel plots of OER currents in (a); (c) Oxygen evolution currents for
35 Co/N-C samples and Pt/C before and after potential sweeps (1.25-1.85 V vs. RHE at 0.1 V/s) for 500 cycles; (d) Oxygen electrode activities within the ORR and OER potential window of Co/N-C samples and Pt/C catalysts dispersed on glass carbon electrode in O_2-saturated 0.1 M KOH.

To study the electrocatalytic activity of Co/N-C-800 in OER,
40 linear sweep voltammetry (LSV) measurements were conducted with the same catalysts loaded on the glassy carbon electrodes in

an O_2-saturated 0.1 M KOH (see Experimental Section for details). As comparisons, similar measurements for the commercial Pt/C catalyst, the Co/N-C-800-250 and Co/N-C-800-
45 450 composites were also performed. The ohmic potential drop (iR) losses that arise from the solution resistance were all corrected (Supporting Information, Figure S9). In Fig. 6a, the polarization curves from all the Co/N-C samples show a much earlier onset potential and greater current density than that of Pt/C,
50 indicating high catalytic activity in OER for all the Co/N-C samples. Notably, although the Co/N-C-800 composite exhibits an onset potential similar to those of Co/N-C-800-250 and Co/N-C-800-450 composites, the current density for Co/N-C-800 is the highest among all the Co/N-C samples, implying an excellent
55 catalytic activity for OER arises from the Co NPs embedded in N-doped carbon. Activities for the OER are judged by the potential required to oxidize water at a current density of 10 mA cm^{-2}, which is a convention commonly used in the OER literature, and a metric relevant to solar fuel synthesis.[6] Remarkably, the
60 Co/N-C-800 composite can afford such current density at a small η of 371 mV (compared with the standard reaction potential), which is much smaller than those of other Co/N-C samples and the commercial Pt/C catalyst (Fig. 6a, Table 1), and even comparable with the performance of the best reported carbon
65 supported Co-based OER catalysts: Co_3O_4-RGO (310 mV),[2] Co_3O_4-mMWCNTs (390 mV),[54] and CoO-N-CG (340 mV).[5] The OER kinetics of the above catalysts are studied by plotting their Tafel curves, as shown in Fig. 6b. The resulting Tafel slopes are found to be ~61.4, ~74.1, ~116.1 and ~169.6 mV dec^{-1} for Co/N-
70 C-800, Co/N-C-800-250, Co/N-C-800-450, and the commercial Pt/C, respectively (Fig. 6b, Table 1). Here the Co/N-C-800 composite exhibits the smallest Tafel slope and is therefore the most efficient OER catalyst among all the samples in this study. Notably, such a Tafel slope is even smaller than those of the best
75 reported carbon supported Co-based OER catalysts: Co_3O_4-RGO (67 mV dec^{-1}),[2] Co_3O_4-mMWCNTs (65 mV dec^{-1}),[54] and CoO-N-CG (71 mV dec^{-1}),[5] suggesting the outstanding intrinsic OER kinetics of this kind of N-doped carbon supported cobalt nanoparticles.
80 To investigate the catalyst durability for OER, we performed accelerated stability tests in O_2-saturated 0.1 M KOH at room temperature for the Co/N-C-800 composite with other Co/N-C samples and Pt/C as references. As shown in Fig. 6c, after 500 cycles, the Co/N-C-800 composite exhibits a mere 9 mV increase
85 in η to achieve the current density of 10 mA cm^{-2}, while the same experiment leads to a 20 mV and 14 mV η increase for Co/N-C-800-250 and Co/N-C-800-450, and even a failure to reach such current density for Pt/C, demonstrating the superior durability of the Co/N-C-800 composite catalyst.
90 To better compare and understand the bifunctional catalytic ability, the potential and overpotential (η) at a current density of 10 mA cm^{-2}, the Tafel slope for OER as well as the potential at a current density of -3 mA cm^{-2} for ORR of the above catalysts were all presented in Table 1. It is convenient to estimate the
95 overall electrocatalytic activity of a bifunctional electrocatalyst as an oxygen electrode in alkaline electrolyte by taking the difference in potential between the OER current density at 10 mA cm^{-2} and ORR current density at -3 mA cm^{-2}. The smaller the difference, the better is the potential of the material to be used for

Table 1. Comparison of bifunctional oxygen electrode activity data for different catalysts in this study[a].

Catalysts	η (mV) at J = 10 mA cm^{-2}	Tafel slope (OER) (mV dec^{-1})	E$_{OER}$ (V) at J = 10 mA cm^{-2}	Tafel slope (ORR) (mV dec-1)	E$_{ORR}$ (V) at J = -3 mA cm^{-2}	Oxygen electrode ΔE (V) = E$_{OER}$ - E$_{ORR}$
Co/N-C-800	371	61.4	1.599	61	0.74	0.859
Co/N-C-800-250	424	116.1	1.652	68	0.712	0.94
Co/N-C-800-450	398	74.1	1.626	80	0.099	1.527
Pt/C	629	169.6	1.857	68	0.784	1.073

[a] All the potential values here were vs. RHE for comparison.

practical applications. The oxygen electrode activities for the above catalysts are shown in Fig. 6d and the values are also listed in Table 1. The oxygen electrode activities (ΔE) for Co/N-C-800, Co/N-C-800-250, Co/N-C-800-450, and the commercial Pt/C are calculated to be 0.859, 0.94, 1.527 and 1.073 V respectively, demonstrating the bifunctional catalytic activities of Co/N-C samples following an order of Co/N-C-800 > Co/N-C-800-250 > Co/N-C-800-450. More importantly, such a ΔE value for Co/N-C-800 is even smaller than Ir/C, Ru/C and most of the non-precious metal based bifunctional electrocatalysts reported in previous literatures (Supporting Information, Table S2),[6, 11, 18, 19, 21, 22, 55] indicating the excellent bifunctional activity of the Co/N-C-800 composite.
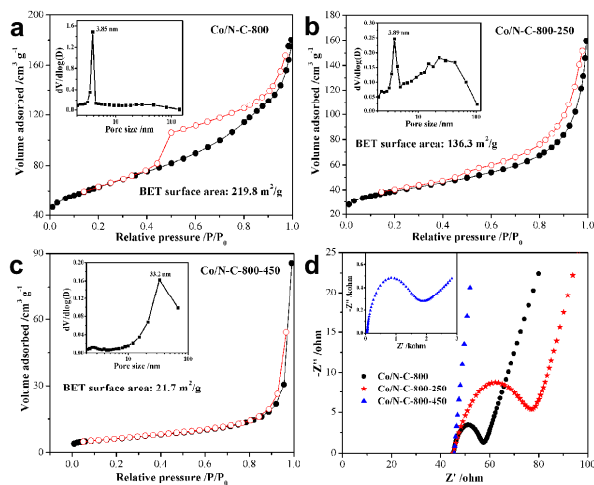

Fig. 7 Nitrogen absorbtion and desorption isotherms of (a) Co/N-C-800, (b) Co/N-C-800-250, and (c) Co/N-C-800-450, the insets show the corresponding BJH pore distributions; (d) Nyquist plots of different Co/N-C catalyst-modified electrodes in 0.1 M KOH solution, the inset of (d) shows the complete Nyquist plot of Co/N-C-800-450.

To gain insight into the reason for the better bifunctional catalytic activity of Co/N-C-800 than other Co/N-C samples, nitrogen adsorption-desorption measurements were carried out first. As shown in Fig. 7a, the N$_2$-adsorption isotherm of Co/N-C-800 composite exhibits a type-IV isotherm with a high surface area of 219.8 m^2 g^{-1}. The distinct hysteresis loop in the large range of ca. 0.4-0.8 P/P$_0$ indicates the presence of mesoporous structure, which could also be seen from the pore size distribution (the inset of Fig. 7a): the mesopores with an average value of 3.85 nm.[10, 50, 56] In contrast, the Co/N-C-800-250 composite exhibits a lower BET surface area of 136.3 m^2 g^{-1}, and both a narrow pore-size distribution centered at 3.89 nm and the broad pore-size distribution in the range of 10-50 nm deriving from the desorption data using the BJH model (Fig. 7b and the inset). The

presence of these large mesopores in Co/N-C-800-250 is mainly attributed to the formation of cobalt-oxide nanoparticle aggregates, which causes the generation of interparticular pores and consequently decreases the BET surface area,[20] as evidenced by the XRD pattern and SEM image of Co/N-C-250 (Fig. 1 and Figure S5a). While for Co/N-C-800-450, a much lower BET surface area of 21.7 m^2 g^{-1} is displayed, and the pore-size distribution centers at a large mesopore size of 33.2 nm (Fig. 7c and the inset). The much lower surface area for Co/N-C-800-450 is owing to the complete conversion of Co NPs to Co$_3$O$_4$ aggregates and the severe decomposition of N-doped carbon, as revealed by the XRD pattern, SEM image and the EDX result of Co/N-C-800-450 (Fig. 1, Figure S5b, Figure S10c). Obviously, the high surface area is mainly attributed to the mesoporous structure. The high specific surface area of Co/N-C-800 could provide higher surface density of catalytic active sites exposed to the ORR- and OER-relevant species (O$_2$, OH$^-$, e$^-$, H$_2$O) and the mesoporous structure could also provide the possibility of efficient mass transport, which lead to enhanced catalytic activity. Then, electrochemical impedance spectroscopy (EIS) measurements were also performed for all the Co/N-C samples, as presented in Fig. 7d. The charge-transfer resistance of Co/N-C-800-250 (32.2 Ω) is nearly three times larger than that of Co/N-C-800 (12.6 Ω), which could be due to the partial oxidation of metallic cobalt to cobalt oxides (CoO & Co$_3$O$_4$) and the slight decomposition of N-doped carbon in Co/N-C-800-250 composite (Fig. 1 and Figure S10b). While for Co/N-C-800-450, owing to the complete conversion of metallic cobalt to Co$_3$O$_4$ and the breaking down of N-doped carbon (Fig. 1 and Figure S10c), a much larger charge-transfer resistance (more than 1500 Ω) is displayed. The small charge transfer resistance of Co/N-C-800 clearly indicates better electronic transport capability than other Co/N-C samples and facilitates more efficient charge transfer process.
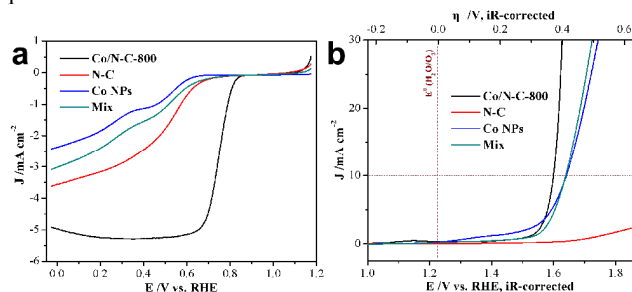

Fig. 8 (a) ORR and (b) OER linear sweep voltammograms at 1600 rpm for Co/N-C-800, N-C, pristine Co NPs, and the physical mixture of N-C and Co NPs (Mix) in O$_2$-saturated 0.1 M KOH.

Further, to better understand and investigate the contributions of N-doped carbon and Co NPs to the catalytic activity of Co/N-

C-800, we prepared N-doped carbon (N-C) (Figure S11) and pristine Co NPs (Figure S12) as control samples and we tested the LSVs of N-C, Co NPs, and physical mixture of N-C and Co NPs (Mix) catalysts for both ORR and OER. As shown in Fig. 8, the pristine Co NPs displays poor ORR activity and high OER activity, N-C manifests relatively high ORR activity and negligible OER activity. While the Co/N-C-800 composite exhibits significantly higher activities than N-C, Co NPs and physical mixture of N-C and Co NPs in both ORR and OER. These results suggest that the high performance of the Co/N-C-800 hybrid composite is a result of collective action by Co NPs and N-doped carbon in the hybrid as a whole, namely, there exists a synergistic effect between Co NPs and N-C in the Co/N-C-800 hybrid composite. While for Co/N-C-800-250 and Co/N-C-800-450, the synergistic interactions between Co NPs and N-C would be weakened and even destroyed due to the oxidation conversion of Co NPs to cobalt oxides (CoO & Co_3O_4) and the decomposition of N-doped carbon in the composites.

Therefore, apart from the high specific surface area and the small charge transfer resistance, the good synergistic interaction between Co NPs and N-C in Co/N-C-800 composite also plays an important role in enhancing the bifunctional catalytic activity of the composite. Then, on the whole, it can be concluded that the high specific surface area, small charge transfer resistance and good synergistic interaction could be the causes for the better bifunctional catalytic activity of Co/N-C-800 than other Co/N-C samples.

Conclusions

In summary, via a solvothermal carbonization approach, a hybrid composite of Co NPs embedded in N-doped carbon (Co/N-C-800) has been synthesized. With the synergistic effect arised from the N-doped carbon and Co NPs in the composite, the Co/N-C-800 hybrid catalyst exhibits highly efficient bifunctional catalytic activity and excellent durability for both ORR and OER, even better than Pt/C and most of the non-precious metal bifunctional catalysts in previous literatures. Furthermore, the Co/N-C-800 composite also shows better bifunctional catalytic activity than its oxidative counterparts, which could be attributed to the high specific surface area and efficient charge transfer ability of the composite, as well as the good synergistic effect between N-doped carbon and the Co NPs in the Co/N-C-800 composite. We believe that the novel Co/N-C hybrid catalyst will facilitate the development of next-generation ORR and OER processes with carbon based hybrid materials, and it is anticipated that the Co/N-C-800 composite used as a bifunctional electrocatalyst in URFC would offer a competitive advantage over the conventional precious metal catalysts.

Acknowledgements

Notes and references

55 *Key Laboratory for Ultrafine Materials of Ministry of Education, School of Materials Science and Engineering, East China University of Science and Technology, 130 Meilong Road, Shanghai 200237, China. Fax: +86 21 64250624; Tel: +86 21 64252022; Email: yhzhu@ecust.edu.cn (Y. Zhu), jiandingchen@ecust.edu.cn (J. Chen).*

60 † Electronic Supplementary Information (ESI) available: Detailed and additional Figures as noted in the text. See DOI: 10.1039/b000000x/
1. M. Winter and R. J. Brodd, *Chem. Rev.*, 2004, **104**, 4245-4270.
2. Y. Liang, Y. Li, H. Wang, J. Zhou, J. Wang, T. Regier and H. Dai, *Nat. Mater.*, 2011, **10**, 780-786.
65 3. A. Kudo and Y. Miseki, *Chem. Soc. Rev.*, 2009, **38**, 253-278.
4. K. Maeda, K. Teramura, D. Lu, T. Takata, N. Saito, Y. Inoue and K. Domen, *Nature*, 2006, **440**, 295-295.
5. S. Mao, Z. Wen, T. Huang, Y. Hou and J. Chen, *Energy Environ. Sci.*, 2014, **7**, 609-616.
70 6. Y. Gorlin and T. F. Jaramillo, *J. Am. Chem. Soc.*, 2010, **132**, 13612-13614.
7. J. Suntivich, K. J. May, H. A. Gasteiger, J. B. Goodenough and Y. Shao-Horn, *Science*, 2011, **334**, 1383-1385.
8. B. S. Yeo and A. T. Bell, *J. Am. Chem. Soc.*, 2011, **133**, 5587-5593.
75 9. G. Chen, S. R. Bare and T. E. Mallouk, *J. Electrochem. Soc.*, 2002, **149**, A1092-A1099.
10. Y. Tan, C. Xu, G. Chen, X. Fang, N. Zheng and Q. Xie, *Adv. Funct. Mater.*, 2012, **22**, 4584-4591.
11. C. Jin, F. Lu, X. Cao, Z. Yang and R. Yang, *J. Mater. Chem. A*, 2013,
80 **1**, 12170-12177.
12. G.-L. Tian, M.-Q. Zhao, D. Yu, X.-Y. Kong, J.-Q. Huang, Q. Zhang and F. Wei, *Small*, 2014, **10**, 2251-2259.
13. Z. Chen, D. Higgins, A. Yu, L. Zhang and J. Zhang, *Energy Environ. Sci.*, 2011, **4**, 3167-3192.
85 14. H. Yamazaki, A. Shouji, M. Kajita and M. Yagi, *Coordin. Chem. Rev.*, 2010, **254**, 2483-2491.
15. F. Cheng, Y. Su, J. Liang, Z. Tao and J. Chen, *Chem. Mater.,* 2009, **22**, 898-905.
16. Y. Feng, T. He and N. Alonso-Vante, *Chem. Mater.*, 2007, **20**, 26-28.
90 17. D. Zhao, S. Zhang, G. Yin, C. Du, Z. Wang and J. Wei, *J. Power Sources*, 2012, **206**, 103-107.
18. D. Wang, X. Chen, D. G. Evans and W. Yang, *Nanoscale*, 2013, **5**, 5312-5315.
19. M. Prabu, K. Ketpang and S. Shanmugam, *Nanoscale*, 2014, **6**, 3173-3181.
95 20. W. Chaikittisilp, N. L. Torad, C. Li, M. Imura, N. Suzuki, S. Ishihara, K. Ariga and Y. Yamauchi, *Chem. Eur. J.*, 2014, **20**, 4217-4221.
21. D. U. Lee, B. J. Kim and Z. Chen, *J. Mater. Chem. A*, 2013, **1**, 4754-4762.
100 22. Q. Liu, J. Jin and J. Zhang, *ACS Appl. Mater. Interfaces*, 2013, **5**, 5002-5008.
23. X. Zhai, W. Yang, M. Li, G. Lv, J. Liu and X. Zhang, *Carbon*, 2013, **65**, 277-286.
24. Y. Liang, H. Wang, P. Diao, W. Chang, G. Hong, Y. Li, M. Gong, L.
105 Xie, J. Zhou, J. Wang, T. Z. Regier, F. Wei and H. Dai, *J. Am. Chem. Soc.*, 2012, **134**, 15849-15857.
25. J. Xu, P. Gao and T. S. Zhao, *Energy Environ. Sci.*, 2012, **5**, 5333-5339.
26. Y. Su, Y. Zhu, X. Yang, J. Shen, J. Lu, X. Zhang, J. Chen and C. Li,
110 *Ind. Eng. Chem. Res.*, 2013, **52**, 6076-6082.
27. J. Liu, L. Jiang, Q. Tang, B. Zhang, D. S. Su, S. Wang and G. Sun, *ChemSusChem*, 2012, **5**, 2315-2318.
28. H. Wang, Y. Liang, Y. Li and H. Dai, *Angew. Chem. Int. Ed.*, 2011, **50**, 10969-10972.
115 29. Z. Zhuang, W. Sheng and Y. Yan, *Adv. Mater.*, 2014, **26**, 3950-3955.
30. C. Zhao, D. Li and Y. Feng, *J. Mater. Chem. A*, 2013, **1**, 5741-5746.
31. J. Rosen, G. S. Hutchings and F. Jiao, *J. Am. Chem. Soc.*, 2013, **135**, 4516-4521.
32. M. W. Kanan and D. G. Nocera, *Science*, 2008, **321**, 1072-1075.
120 33. Y. Yao, C. Xu, J. Qin, F. Wei, M. Rao and S. Wang, *Ind. Eng. Chem. Res.*, 2013, **52**, 17341-17350.
34. S. Guo, S. Zhang, L. Wu and S. Sun, *Angew. Chem. Int. Ed.*, 2012, **51**, 11770-11773.
35. K. Ai, Y. Liu, C. Ruan, L. Lu and G. M. Lu, *Adv. Mater.,* 2013, **25**,
125 998-1003.

36. M.-R. Gao, X. Cao, Q. Gao, Y.-F. Xu, Y.-R. Zheng, J. Jiang and S.-H. Yu, *ACS Nano*, 2014, **8**, 3970-3978.
37. U. A. Paulus, T. J. Schmidt, H. A. Gasteiger and R. J. Behm, *J. Electroanal. Chem.*, 2001, **495**, 134-145.
5 38. Y. Su, H. Jiang, Y. Zhu, X. Yang, J. Shen, W. Zou, J. Chen and C. Li, *J. Mater. Chem. A*, 2014, **2**, 7281-7287.
39. L. Lai, J. R. Potts, D. Zhan, L. Wang, C. K. Poh, C. Tang, H. Gong, Z. Shen, J. Lin and R. S. Ruoff, *Energy Environ. Sci.*, 2012, **5**, 7936-7942.
10 40. H. Niwa, K. Horiba, Y. Harada, M. Oshima, T. Ikeda, K. Terakura, J.-i. Ozaki and S. Miyata, *J. Power Sources*, 2009, **187**, 93-97.
41. B. Zheng, J. Wang, F.-B. Wang and X.-H. Xia, *Electrochem. Commun.*, 2013, **28**, 24-26.
42. Y. Xiao, C. Hu, L. Qu, C. Hu and M. Cao, *Chem. Eur. J.*, 2013, **19**, 14271-14278.
15 43. Y. Hu, J. O. Jensen, W. Zhang, L. N. Cleemann, W. Xing, N. J. Bjerrum and Q. Li, *Angew. Chem. Int. Ed.*, 2014, **53**, 3675-3679.
44. G. Wu, K. L. More, C. M. Johnston and P. Zelenay, *Science*, 2011, **332**, 443-447.
20 45. M. Ibrahim, C. Marcelot-Garcia, K. Aït Atmane, E. Berrichi, L.-M. Lacroix, A. Zwick, B. Warot-Fonrose, S. Lachaize, P. Decorse, J.-Y. Piquemal and G. Viau, *J. Phys. Chem. C*, 2013, **117**, 15808-15816.
46. D. Xu, P. Lu, P. Dai, H. Wang and S. Ji, *J. Phys. Chem. C*, 2012, **116**, 3405-3413.
25 47. M. P. Hyman and J. M. Vohs, *Surf. Sci.*, 2011, **605**, 383-389.
48. V. Datsyuk, M. Kalyva, K. Papagelis, J. Parthenios, D. Tasis, A. Siokou, I. Kallitsis and C. Galiotis, *Carbon*, 2008, **46**, 833-840.
49. I.-Y. Jeon, S. Zhang, L. Zhang, H.-J. Choi, J.-M. Seo, Z. Xia, L. Dai and J.-B. Baek, *Adv. Mater.*, 2013, **25**, 6138-6145.
30 50. H. Jiang, Y. Su, Y. Zhu, J. Shen, X. Yang, Q. Feng and C. Li, *J. Mater. Chem. A*, 2013, **1**, 12074-12081.
51. Z.-S. Wu, S. Yang, Y. Sun, K. Parvez, X. Feng and K. Müllen, *J. Am. Chem. Soc.*, 2012, **134**, 9082-9085.
52. C. Zhang, R. Hao, H. Yin, F. Liu and Y. Hou, *Nanoscale*, 2012, **4**, 7326-7329.
35 53. H. Yin, C. Zhang, F. Liu and Y. Hou, *Adv. Funct. Mater.*, 2014, **24**, 2930-2937.
54. X. Lu and C. Zhao, *J. Mater. Chem. A*, 2013, **1**, 12053-12059.
55. W. G. Hardin, D. A. Slanac, X. Wang, S. Dai, K. P. Johnston and K. J. Stevenson, *J. Phys. Chem. Lett.*, 2013, **4**, 1254-1259.
40 56. H.-W. Liang, W. Wei, Z.-S. Wu, X. Feng and K. Müllen, *J. Am. Chem. Soc.*, 2013, **135**, 16002-16005.

Nanoscale Accepted Manuscript